Supplementary Material

STRUCTURE OF LOW-ORDER HEMIMORPHITE PRODUCED IN A ZN-RICH ENVIRONMENT BY CYANOBACTERIUM *LEPTOLINGBYA FRIGIDA*

DANIELA MEDAS[1], CARLO MENEGHINI[2], FRANCESCA PODDA[1], COSTANTINO FLORIS[1], MARIANO CASU[1], MARIA ANTONIETTA CASU[3], ELODIA MUSU[4], GIOVANNI DE GIUDICI[1,*]

[1]Department of Chemical and Geological Sciences, University of Cagliari, S.S. 554, 09042 Monserrato, Cagliari, Italy

[2] Department of Sciences, University of Roma Tre, Via della Vasca Navale 84, 00146 Rome, Italy

[3] National Research Council, Institute of Translational Pharmacology, UOS of Cagliari, Scientific and Technological Park of Sardinia - POLARIS, 09010 Pula, Cagliari, Italy

[4] CRS4- Microlab Scientific and Technological Park of Sardinia, 09010 Pula, Cagliari, Italy

*E-mail: gbgiudic@unica.it

LIST OF CONTENTS

S1. X-ray Absorption Spectroscopy Analysis

Samples were prepared in form of self-supported pellets by mixing sample powders (about 16 mg) and pure cellulose (about 100 mg), then pressing at 5 kbar for few minutes. XAS spectra were measured in transmission geometry keeping the sample at liquid nitrogen (TLN~80 K) in order to minimize the thermal disorder effect on the XAS structural signal. The incident, I_o, and transmitted, I_t, X-ray beam intensities were detected using ionization chamber with opportune gas mixture (Ar, N_2 and He) to give 20% absorption at I_0 and 80% absorption at I_1 chamber. After I_1 the absorption spectrum from a reference Zn foil was measured using a third ionization chamber (I_2) in order to monitor the x-ray beam energy calibration.

Standard procedures (Rehr and Albers 2000) were used for XAS data normalization and extracting the structural EXAFS (Extended X-ray Absorption Fine Structure) signal $\chi(k)$ using ESTRA code (Meneghini et al. 2012); these procedures include pre-edge linear back-ground removal, spline modelling of bare atomic background μ_o, and edge step normalization. Third degree polynomial splines (roughly spaced $\Delta k \sim 3$ Å^{-2}) were used to model the post-edge background μ_o. The photoelectron wavevector modulus k ($k = \sqrt{\frac{2m}{\hbar^2}(E - E_o)}$), was calculated choosing the edge energy (E_o) at the first inflection point (first derivative maximum) of the absorption spectrum, and refined during the data fitting.

The EXAFS data refinement was performed using the FITEXA code (Meneghini et al. 2012) which exploits the MINUIT routines (CERN Fortran libraries) (James 1994) for versatile least square refinement and accurate statistical error analysis. Data refinement was performed on the raw $k\chi(k)$ spectra (i.e. without Fourier filtering), applying the standard EXAFS formula (Rehr and Albers 2000). Model atomic clusters obtained from crystallographic models (ICSD) were used to calculate theoretical amplitude and phase functions with FEFF 8.4 code (Zabinsky et al. 1995; Ankudinov et al. 1998). The atomic structure of crystallographic model was the starting points for the data refinements. Usually, for each spectrum, coordination numbers (CN), bond distances (R), and mean square relative displacement (MSRD) factors (σ^2) were let free to vary for each shell. Physical constraints were applied in order to reduce the number of free parameters: in each refinement the same edge energy shift (ΔE) was applied to all considered shells. Standard errors on the refined parameters are calculated using the MINOS option in the program (James 1994), which also takes into account the correlation between

parameters. In order to evaluate the best fit quality, we report in tables also the R^2 factor:

$$R^2 = \frac{\sum_i \left(\chi(k_i) - \chi_{th}(k_i)\right)^2}{\sum_i \left(\chi(k_i)\right)^2}$$

quantifying the absolute misfit between experimental data and theory (Standards and Criteria Committee 2000). Here $\chi(k_i)$ and $\chi_{th}(k_i)$ are respectively the experimental data and the theoretical values at the point k_i and the sum runs over all the experimental data points.

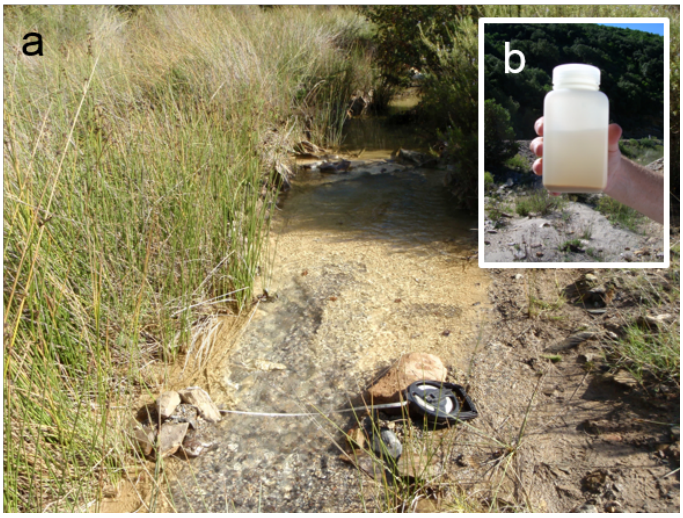

Figure S1. Zn silicate biomineral along the Naracauli stream (a), and collected by a high-density polyethylene bottle (b).

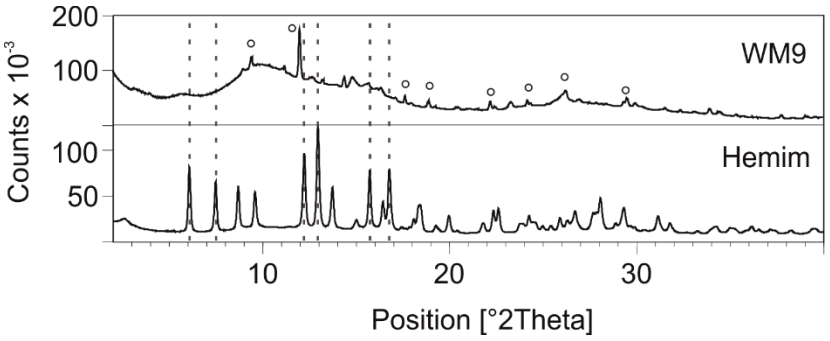

Figure S2. X-ray diffraction patterns of biomineral sample WM9 collected along the Naracauli stream and abiotic hemimorphite from San Giovanni Mine (Sardinia, Italy). Dashed lines indicate the main peaks of hemimorphite and circles indicate the peaks of quartz. The WM9 pattern has been collected at the BM08 beamline (Meneghini et al. 2001) of the European Synchrotron Radiation Facility (ESRF, Grenoble, France) using an angle dispersed set-up based on a large area detector, especially suited for high statistics XRD data.

S2. FTIR analysis

Figure 2 shows the FTIR spectra of the samples WM9, WM13 in the range 400–4000 cm^{-1}. The two spectra are very similar, however in the spectrum of WM13 it is observed that the peaks at 1391 cm^{-1} and at 559 cm^{-1} are more intense than in the sample WM9. A broad band between 3700 – 2800 cm^{-1} and a less intense absorption at 1647 cm^{-1} can be assigned to the adsorbed water or crystallization water (Nakamoto, 1986). The presence of intense peaks in the range 1550 and 1370 cm^{-1} can be attributed to the presence of carbonate stretching. This is confirmed by the peaks at 1050 cm^{-1}, ν1 symmetric CO_3^{2-} stretching mode, peaks at 834 cm^{-1}, ν2 out-of-plane OCO bending mode. The presence of the peak at 467 cm^{-1}, attributed to Zn-O bending mode, allows to assign all these characteristic peaks to hydrozincite (Music et al. 2002; Stoilova et al. 2002; Hales and Frost 2007). The FTIR spectra of pure hydrozincite and hemimorphite are shown for comparison.

S3. ^{29}Si NMR analysis

In the ^{1}H-^{29}Si cross-polarization experiment, magnetization transfer to the Si nucleus depends upon the contact time period and is related to other structure-dependent parameters, such as the distance between the two nuclei, the number of protons, and the proton relaxation times in the rotating frame (Mehring 1983; Slichter 1989). Only signals from Si atoms having neighboring hydrogen atoms can be collected in the cross-polarization spectrum.

S4. ^{13}C NMR analysis

During the ^{1}H-^{13}C cross-polarization experiment the proton magnetization is transferred to a carbon nucleus during the contact time period; this transfer is correlated to the distance between the proton and the carbon nuclei and is governed by characteristic proton spin-lattice relaxation time in the rotating frame (T1ρ) and the carbon-proton cross polarization time (Mehring 1983; Slichter 1989). A quaternary or poorly protonated carbon is normally affected by slow rates of cross polarization from the few bonded or remote protons (Mehring 1983; Slichter 1989; Alemany et al. 1983).

Spectra of the biomineral samples (see Fig. 4 in the main paper) show a signal at 166.8 ppm, full width at half maximum of 3.6 ppm. According to the FTIR spectra, the signal at 166.8 ppm can be attributed to the carbonate group of hydrozincite (De Giudici et al. 2009; Scorciapino et al. 2013). In a previous study on the biomineral hydrozincite, it was shown that the ^{13}C NMR spectra are characterized by the presence of more than one peak in the range 160-168 ppm (De Giudici et al. 2009). Medas et al. (2014) suggested that hydrozincite observed in WM samples is detrital. In fact, hydrozincite in these samples occurs as sparse fragments not connected to the extracellular polymeric substances secreted by the cyanobacteria *Leptolyngbya frigida*. For this reason, the presence of hydrozincite was no further considered in the discussion section of the main paper.

S5. X-ray Absorption Spectroscopy results

The best fits obtained with and without the Si shell are reported in Fig. S2 for sake of completeness. The statistical analysis (Meneghini et al. 2012) demonstrates that adding the Si shell improve the best fit quality reducing the R^2 by about 50 %. Noticeably in the previous data (Medas et al. 2014), the statistical analysis did not permit to reliably assess the presence of such a Zn-Si shell. Here the Zn-Si shell resulted statistically significant thanks to a better data quality that allowed to extend the k-range of EXAFS data analysis. We checked the possibility to add further coordination shells in the analysis but the improvement of the best fit resulted not statistically significant.

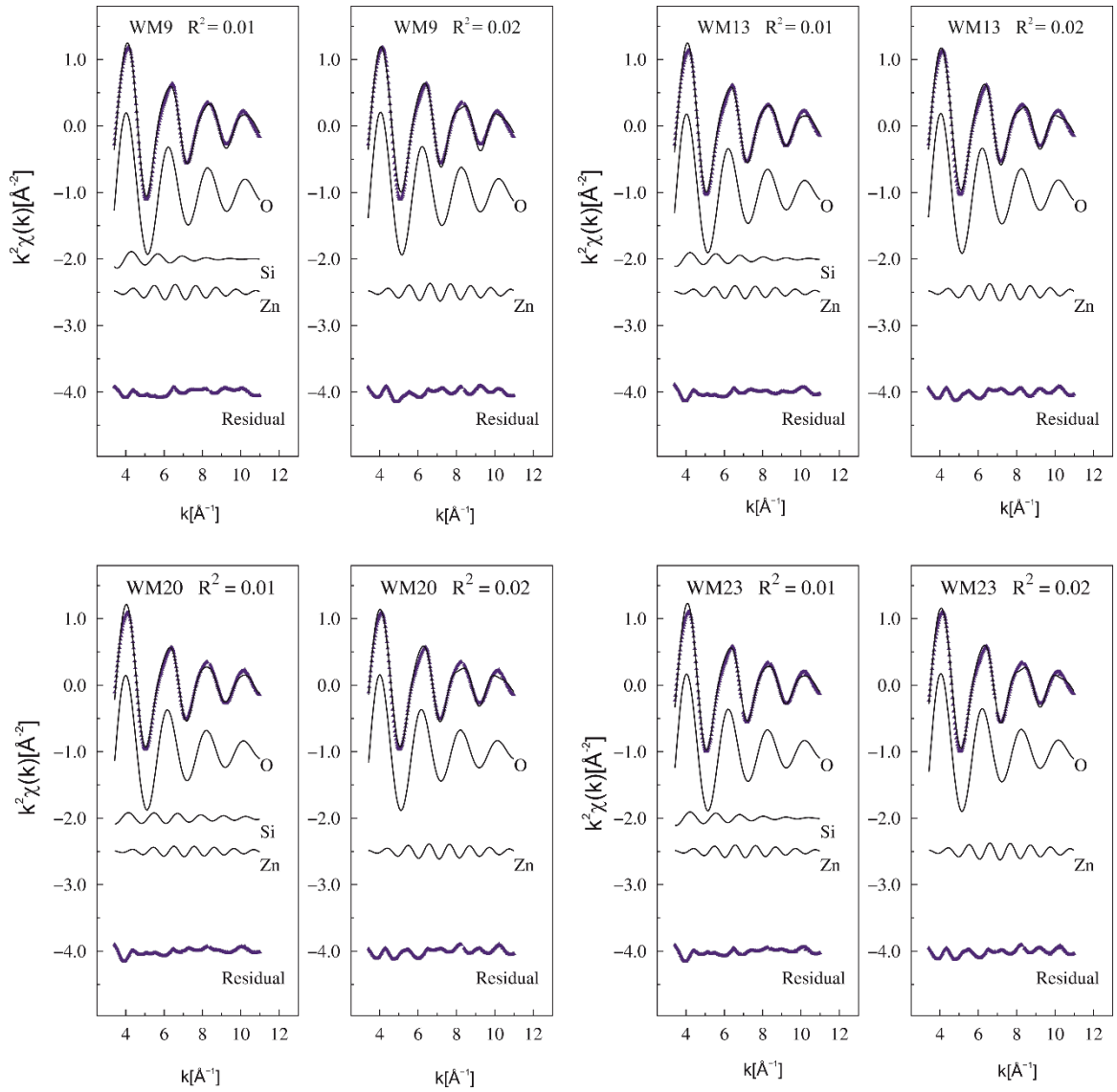

Figure S3. Experimental data (points) and best fits (full lines) of EXAFS spectra of biomineral samples with and without the Si shell.

Table S1. Results of Loss on Ignition analysis.

Sample	LOI % w/w
WM1	13.08
WM3	15.12
WM4	11.32
WM5	11.31
WM7	12.45
WM9	13.62
WM10	14.55
WM13	11.94
WM14	11.03
WM15	10.74
WM20	10.05
WM21	10.32
WM22	10.01
WM23	9.50

REFERENCES

Alemany, L.B., Grant, D.M., Pugmire, R.J., Alger, T.D., and Zilm, K.W. (1983) Cross polarization and magic angle sample spinning NMR spectra of model organic compounds. 1. Highly protonated molecules. Journal of the American Chemical Society, 105, 2133–2141.

Ankudinov, A.L., Ravel, B., Rehr, J.J., and Conradson, S.D. (1998) Real-space multiple-scattering calculation and interpretation of X-ray-absorption near-edge structure. Physical Review B, 58, 7565–7576.

De Giudici, G., Podda, F., Sanna, R., Musu, E., Tombolini, R., Cannas, C., Musinu, A., and Casu, M. (2009) Structural properties of biologically controlled hydrozincite: An HRTEM and NMR spectroscopic study. American Mineralogist, 94, 1698–1706.

Hales, M.C., and Frost,, R.L. (2007) Synthesis and vibrational spectroscopic characterization of synthetic smithsonite and hydrozincite. Polyhedron, 26, 4955–4962.

James, F. (1994) MINUIT: Function Minimization and Error Analysis. Reference Manual Version 94.1, CERN Program Library D506, 1994.S.

Medas, D., Lattanzi, P., Podda, F., Meneghini, C., Trapananti, A., Sprocati, A.R., Casu, M.A., Musu, E., and De Giudici, G. (2014) The amorphous Zn biomineralization at Naracauli stream, Sardinia: electron microscopy and X-ray absorption spectroscopy. Environmental Science and Pollution Research, 21, 6775–6782.

Meneghini, C., Bardelli, F., and Mobilio, S. (2012) ESTRA-FitEXA: a software package for EXAFS data analysis. Nuclear Instruments and Methods in Physics Research Section B, 285, 153–157.

Mehring, M. (1983) Principles of High Resolution NMR in Solids, 2nd ed., 342 p. Springer-Verlag, New York.

Music, S., Dragcevic, D., Maljkovic, M., and Popovic, S. (2002) Influence of chemical synthesis on the crystallization and properties of zinc oxide. Materials Chemistry and Physics, 77, 521–530.

Nakamoto, K. (1986) Infrared and Raman Spectra of Inorganic and Coordination Compounds. John Wiley and Sons, New York, 1986.

Rehr, J.J., and Albers, R.C. (2000) Theoretical approaches to X-ray absorption fine structure. Reviews of Modern Physics, 72, 621–654.

Scorciapino, M.A., Sanna, R., De Giudici, G., Floris, C., and Casu, M. (2013) Investigation of the hydrozincite structure by infrared and solid-state NMR spectroscopy. American Mineralogist, 98, 1219–1226

Slichter, C.P. (1989) Principles of Magnetic Resonance, 3rd ed., 655 p. Springer Verlag, New York.

Standards and Criteria Committee (2000). http://www.webcitation.org/6jSRyEllc, accessed Aug. 02, 2016.

Stoilova, D., Koleva, V., and Vassileva, V. (2002) Infrared study of some synthetic phases of malachite $Cu_2(OH)_2CO_3$)–hydrozincite ($Zn_5(OH)_6(CO_3)_2$) series. Spectrochimica Acta Part A, 58, 2051–2059.

Zabinsky, S.I., Rehr, J.J., Ankudinov, A., Albers, R.C., and Eller, M.J. (1995) Multiple-scattering calculations of X-ray-absorption spectra. Physical Review B, 52, 2995–3009.